1 **Thermal equation of state of the main minerals of eclogite: Constraining the**

2 **density evolution of eclogite during delamination process in Tibet**

3 Zhilin Ye [a,b], Dawei Fan [a,*], Bo Li [c], Qizhe Tang [d], Jingui Xu [e,*], Dongzhou Zhang [e], Wenge Zhou [a]

4 [a] *Key Laboratory of High-Temperature and High-Pressure Study of the Earth's Interior, Institute of*

5 *Geochemistry, Chinese Academy of Sciences, Guiyang, Guizhou 550081, China*

6 [b] *University of Chinese Academy of Sciences, Beijing 100049, China*

7 [c] *Research Institute of Petroleum Exploration & Development-Northwest (NWGI), PetroChina Lanzhou*

8 *730020, China*

9 [d] *School of Information Engineering, Huzhou University, Huzhou, Zhejiang 313000, China*

10 [e] *Hawaii Institute of Geophysics and Planetology, School of Ocean and Earth Science and Technology,*

11 *University of Hawaii at Manoa, Honolulu, Hawaii 96822, USA*

12 * Corresponding authors:

13 *E-mail addresses*: fandawei@vip.gyig.ac.cn (D. Fan), xujingui@hawaii.edu (J. Xu)

15 **Abstract**

16 Tibet, which is characterized by collisional orogens, has undergone the process of delamination or

17 convective removal. The lower crust and mantle lithosphere appear to have been removed through

18 delamination during orogenic development. Numerical and analog experiments demonstrate that

19 the metamorphic eclogitized oceanic subduction slab or lower crust may promote gravitational

20 instability due to its increased density. The eclogitized oceanic subduction slab or crustal root is

21 believed to be denser than the underlying mantle and tends to sink. However, the density of

22 eclogite under high-pressure and high-temperature conditions and density differences from the

23 surrounding mantle is not preciously constrained. Here, we offer new insights into the derivation

24 of eclogite density with a single experiment to constrain delamination in Tibet. Using *in situ*

25 synchrotron X-ray diffraction combined with diamond anvil cell, experiments focused on minerals

26 (garnet, omphacite, and epidote) of eclogite are conducted under simultaneous high-pressure and

27 high-temperature conditions, which avoids systematic errors. Fitting the pressure-temperature-

28 volume data with the third-order Birch-Murnaghan equation of state, the thermal equation of state

29 (EoS) parameters, including the bulk modulus (K_{T0}), its pressure derivative (K_{T0}'), and the thermal

30 expansion coefficient (α_0), are derived. The densities of rock-forming minerals and eclogite are

31 modeled along with the geotherms of two types of delamination. The delamination processes of

32 subduction slab breakoff and the removal of the eclogitized lower crust in Tibet are discussed. The

33 Tibetan eclogite which containing 40-60 vol. % garnet and 44-70% degrees of eclogitization can

34 promote the delamination of slab break-off in Tibet. Our results indicate that eclogite is a major

35 controlling factor in the initiation of delamination. A high abundance of garnet, a high Fe-content,

36 and a high degree of eclogitization are more conducive to instigating the delamination.

37 **Keywords:**

38 Eclogite, Equation of state, Single-crystal X-ray diffraction, Delamination, Tibet

40 **1. Introduction**

41 The evolution of orogenesis is characterized by lithospheric removal during rapid surface uplift,

42 mantle upwelling, and postcollisional magmatism, particularly in the Central Andes (e.g. Ehlers

43 and Poulsen, 2009), Himalayas (e.g. Singh and Kumar, 2009), and Dabie orogen (e.g. He et al.,

44 2011).

45   It is widely accepted that delamination is the most important mechanism of lithospheric

46   removal. Delamination is induced and accompanied by two major requisites: (a) the density

47   difference caused by the negative buoyancy of the delaminated lithosphere; and (b) the presence

48   of a weak lower crust (lower viscosity) that exists between the strong upper crust and lithospheric

49   mantle. Usually, two types of delamination are believed to occur in orogen development. The first

50   is the conventional definition of delamination proposed by Bird (1978, 1979), which was used to

51   interpret the geodynamic evolution of the Colorado Plateau. In this scenario, mantle lithosphere

52   peels back from the overlying upper crust and is removed entirely, with the rising hot mantle

53   filling the lithospheric removal zone (e.g. Göğüş and Ueda, 2018; Krystopowicz and Currie, 2013).

54   A weak decoupling layer, i.e, the lower crust, is an essential condition in this delamination model,

55   which may be affected by the rheological behavior of the hydration, thermal, and chemical

56   characteristics of the lithosphere (e.g. Morency, 2004). In addition to conventional delamination,

57   an alternative delamination mechanism is convective removal based on the Rayleigh-Taylor-type

58   instability model (Houseman et al., 1981), namely, viscous "dripping". This model postulates that

59   there is sufficient perturbation in the lithospheric mantle, which is ascribed to the strong

60   temperature-dependence of typical mantle rheology, without regard to a specific weak layer (e.g.

61   Conrad and Molnar, 1999; Houseman and McKenzie, 1982).

62   All previous studies attribute the gravitational instability process of lithospheric removal to the

63   negative thermal buoyancy of the cold lithosphere (Conrad and Molnar, 1999; Houseman and

64   McKenzie, 1982) or density contrast between asthenosphere and mantle lithosphere. In any case,

65   the density distribution with lithosphere pressure and temperature (P-T) conditions and chemical

66   composition is of vital importance to understanding the process of lithospheric removal.

67   The Tibetan Plateau is the most representative and prominent collisional orogens. Two types of

68   delamination are proposed to proceed (e.g. Chung et al., 2005; Houseman et al., 1981):

69   lithospheric mantle removal and thickened eclogitized crust removal. The Neo-Tethyan oceanic

70   subduction, India-Asia collision, and Indian continental subduction could be further considered

71   responsible for the abnormal thinning of the mantle lithosphere under Tibet (Chung et al., 2005; Li

72   et al., 2019). The lithospheric removal event in Tibet corresponds to Neo-Tethyan oceanic slab

73   break-off. The mechanism is primarily based on density contrasts between the denser mantle

74   lithosphere and the lighter underlying mantle. Some models reveal that lithospheric removal is

75   induced by the retreating high-density eclogitized lithosphere detached from overlying low-

76   density crust (Faccenda et al., 2009; Li et al., 2016). Other alternative models indicate that

77   thickened eclogitized crust is a potential factor deriving lithospheric removal because the

78   eclogitized crustal root is denser than the underlying mantle and tends to sink (Krystopowicz and

79   Currie, 2013). Regardless of the above types of delamination, the density of eclogite is closely

80   related to delamination. Therefore, Tibet provides an excellent opportunity to understand the role

81   of eclogite density in the process of delamination.

82   An immense amount of concrete research has focused on the origin and appearance of

83   lithospheric mantle removal from different angles, such as geophysical (Ren and Shen, 2008),

84   geological (Chung et al., 2005), petrological (Chung et al., 2005; Turner et al., 1993), numerical

85   and analog experiments (Göğüş and Pysklywec, 2008; Morency, 2004). In particular, numerical

86   and analog experiments are used as prominent methods to simulate the dynamics of delamination

87   (Göğüş and Ueda, 2018). Of these studies, the density behavior occurring during the delamination

88   process has also been investigated intensively following thermodynamic (Semprich et al., 2010),

89   seismic/tomography (Matchette-Downes et al., 2019), and numerical simulations (Li et al., 2016).

90   However, few studies have systematically illuminated the issue of delamination from the

91   perspective of eclogite density. Here, we attempt to offer new insights into the derivation of rock

92   density through the mineral physics method to constrain delamination in Tibet (Ye et al., 2021).

93   Conducting a single experiment under high-pressure and high-temperature conditions, we obtain

94   the equation of state (EoS) of the main minerals of eclogite with fewer systematic errors in the

95   experiment. Furthermore, the newly derived EoS of the main minerals of eclogite, combined with

96   the published EoSs of the main minerals of peridotite (Ye et al., 2021), geothermal lines, and

97   collected eclogite mineral compositions, are further used to elucidate a density evolution model

98   during the delamination process in Tibet. We argue that the EoSs of minerals could be used in a

99   straightforward manner as new constraints on the construction of the density model. Using a

100   simplistic calculation setup, in this study, this density evolution model will shed light on the

101   possibility of delamination during the orogen process.

102

103   **2.   Geological background**

104   The Tibetan Plateau is composed of four terranes from south to north: the Himalaya, Lhasa,

105   Qiangtang, and Songpan-Ganzi terranes (Fig. 1). The birth of the Himalayas and Tibetan Plateau

106   is a consequence of the Indo-Asian collision, which began in the early Cenozoic (Hodges et al.,

107   2001; Wang et al., 2008). The Neo-Tethyan oceanic slab is proposed to have detached from the

108   Indian lithosphere, and the onset of the Indo-Asian collision (DeCelles et al., 2002) particularly

109   occurred in the lower part of the Indian and Lhasa lithospheres. The tectonic evolutionary history

110   of the Lhasa terrane and Tethys Himalayas is essential for revealing the origin of the Himalayan-

111   Tibetan orogen. The subducting Neo-Tethyan slab was thrust into southern Tibet approximately

112   70-65 Ma (Fig. 1b). With the closure of the Neo Tethyan Ocean, the India-Asia continent collision

113   caused compressional deformation in southern Tibet, and a series of collision breakoff events were

114   delineated spanning from 65 Ma to 42 Ma (Chung et al., 2005, 2009; Ma et al., 2014; Zhu et al.,

115   2015). During this period, the Indian continental lithosphere might have dragged down to deeper

116   depths during subduction. Meanwhile, slab rollback accompanied by the southward migration of

117   asthenospheric convection in Tibet changed the thermal structure of the mantle wedge. The

118   breakoff of the oceanic Neo-Tethyan slab from the more buoyant Indian continental lithosphere

119   indicated by the eruption of early Eocene Linzizong volcanic rocks in the Gangdese arc or the

120   cessation of Gangdese arc magmatism occurred at ~45 Ma (DeCelles et al., 2002), which opened a

121   channel for the upwelling asthenosphere (Chung et al., 2009; Ma et al., 2014; Zhu et al., 2015).

122   Additionally, geophysical evidence of longitudinal wave (V_P) tomography is interpreted for the

123   north-dipping high-speed anomaly, which is ascribed to the deep Indian mantle lithosphere (Li et

124   al., 2008). Subsequently, the subduction of the Indian continental margin continues at a low

125   subduction angle beneath the Lhasa terrane (Guillot et al., 2008).

126   In addition, 25 Ma to 0 Ma is another period considered to contain either the occurrence of slab

127   breakoff (Miller et al., 1999) or lithospheric mantle removal following slab breakoff (Chung et al.,

128   2005; Nomade et al., 2004). Previous studies suggested that the hotter asthenosphere considerably

129   raised the geothermal conditions during this period (Chung et al., 2005). Magmatism of the

130   ultrapotassic, shoshonitic, and calc-alkaline was widespread, which was potentially due to the

131   partial melts of the metasomatized lithospheric mantle and eclogitized lower crust. An adopted

132   model of convective lithospheric removal below Lhasa is widely followed (Miller et al., 1999).

133   The lithospheric removal-related mantle upwelling process has been supported by geological,

134   geophysical, and petrological studies (Chung et al., 2005; Ren and Shen, 2008; Turner et al., 1993).

135   Here, slab breakoff and convective lithospheric removal under Tibet are adopted as the

136   background in this study to discuss the possibility of the delamination process.

137

138   ## 3.   Materials and methods

139   ### 3.1 Starting material

140   Natural garnet, omphacite, and epidote samples are collected from eclogite in the Dabie-Sulu

141   ultra-high pressure metamorphic (UHPM) belt. The compositions of each mineral are determined

142   to be $Prp_{21}Alm_{47}Grs_{31}Sps_1$ (Prp = pyrope, Alm = almandine, Grs = grossular, and Sps =

143   spessartine) for garnet, $Quad_{48}Jd_{45}Ae_7$ (Quad = Ferrosilite + enstatite + wollastonite, Jd = jadeite,

144   Ae = aegirine) for omphacite, and $Ca_{2.02}Fe_{0.75}Al_{2.32}Si_{0.16}[SiO_4][Si_2O_7]O(OH)$ for epidote. The

145   compositions of garnet and omphacite are shown in Figure 2 and are within the range of natural

146   mineral compositions of eclogite from Tibet. The chemical composition of representative epidote

147   minerals in Tibet shows that the Fe content of epidote exposed in eclogite is in the range of 0.13-

148   0.25 ($X_{Fe}=Fe^{3+}/(Fe^{3+}+Al^{3+})$) (Huang et al., 2015; Li et al., 2017; Liu et al., 2016), while the Fe

149   content of epidote in this study is 0.24, which is within the Fe content range of natural epidote.

150   The samples used in this study are representative of garnet, omphacite, and epidote minerals in

151   natural eclogites from Tibet. The garnet, omphacite, and epidote with high-quality grains are

152   separated from the eclogite specimens. The above three samples are crushed into 30×40 μm^2 chips

153   with a single crystal thickness of 15 μm in our experiment.

154   ### 3.2 Synchrotron X-ray diffraction

155   The high-pressure and high-temperature experiment is conducted by a BX90 externally-heated

156   diamond anvil cell (EHDAC) with $\pm 15°$ opening angles. The above three single crystals are

157   loaded into the BX90 EHDAC equipped with a pair of 500 μm culet-size diamond anvils and

158   tungsten carbide (WC) seats (Figure S1). The rhenium (Re) gasket is pre-indented to a thickness

159   of ~60 μm, and a cylindrical hole with a diameter of 360 μm is drilled as a sample chamber. Gold

160   powder is also loaded as the pressure calibrant (Fei et al., 2007), and neon is loaded as the

161   pressure transmitting medium through the GeoSoilEnviroCARS (GSECARS) gas loading system

162   (Rivers et al., 2008). The quasi-hydrostatic condition in the sample chamber can be maintained up

163   to ~20 GPa using the neon pressure transmitting medium (Finkelstein et al., 2017). On the other

164   hand, high temperature can significantly decrease the deviatoric stress conditions in the sample

165   chamber. Moreover, previous studies demonstrate that the deviatoric stress disappears at the

166   temperatures of 650 K with neon as the pressure transmitting medium (Klotz et al., 2009; Meng et

167   al., 1993). Therefore, the hydrostatic/quasi-hydrostatic conditions can be maintained within the *P-*

168   *T* range of our experiment (~700 K, 25 GPa). An automated pressure-driven membrane system is

169   utilized to generate increasing pressure up to 25.6 GPa. High-temperature conditions up to 700 K

170   are provided by the heating resistor. Before collecting data, the temperature in the sample chamber

171   will be stabilized for 5 minutes and the temperature fluctuation is less than 1 K. Setup details for

172   the employed thermocouples and heaters can be found in our previous articles (Xu et al., 2019,

173   2020b; Ye et al., 2021).

174   *In-situ* synchrotron single-crystal X-ray diffraction (XRD) experiments were performed at

175   experimental station 13-BM-C of the Advanced Photon Source, Argonne National Laboratory. The

176   detailed experimental process and associated parameters can be seen in our previous studies (Xu et

177   al., 2017, 2018, 2020a; Zhang et al., 2017a). The diffraction images and the lattice parameters

178   were analyzed by the Bruker APEX3 software package (Dera et al., 2013). The representative

179   single-crystal X-ray diffraction patterns are shown in Figure S2. The specific unit-cell parameters

180   of the above three samples at each *P-T* condition can be found in Table S1.

181

182   **4   Results and discussions**

183   **4.1 EoS of main minerals for eclogite**

184   The pressure-volume-temperature (*P-V-T*) data in this study are fitted by the third-order Birch-

185   Murnaghan-EoS (BM3-EoS) (Birch, 1947) in combination with the Holland-Powell thermal-

186   pressure EoS (Holland and Powell, 2011) to obtain the thermal EoS parameters. The volume is

187   calculated in *P-T* space starting with an isothermal compression and followed by a path along an

188   isochor curve to the final temperature. The pressure at a given volume and temperature consists of

189   the following two parts:

$$P(V,T) = P(V,T_0) + P_{th}(V,T) \tag{1}$$

191   The first term corresponds to the pressure calculated by the BM3-EoS for compression at room

192   temperature (*T₀*). The zero-pressure volume (*V_{T0}*), the isothermal bulk modulus (*K_{T0}*), and its

193   pressure derivate (*K_{T0}′*) with the following form:

$$P(V,T_0) = (3/2)K_{T0}\left[\left(V_{T0}/V\right)^{7/3} - \left(V_{T0}/V\right)^{5/3}\right] \times \left\{1 + (3/4)\left(K_{T0}' - 4\right)\left[\left(V_{T0}/V\right)^{2/3} - 1\right]\right\}$$

$$\tag{2}$$

196   The second term is the additional pressure generated by heating along an isochor. The thermal-

197   pressure is following the equation:

$$P_{th}(V,T) = \alpha_{V,0} K_{T0} \left(\frac{\theta_E}{\xi_0}\right)\left(\frac{1}{\exp(\theta_E/T) - 1} - \frac{1}{\exp(\theta_E/T_0) - 1}\right) \tag{3}$$

199 where $\xi = \dfrac{(\theta_E/T)^2 \exp(\theta_E/T)}{((\theta_E/T)-1)^2}$, ξ_0 is the value of ξ at the reference temperature T_0 and $\alpha_{V,0}$ is

200 the thermal expansion coefficient at room temperature. The Einstein temperature θ_E in this study

201 are selected and recalculated from the literature (Faccincani et al., 2021; Gottschalk, 2004).

202   The thermal EoS parameters are derived using the EoSFit program at high-pressure and room-

203 temperature and high-pressure and high-temperature conditions (Angel et al., 2014) and are shown

204 in Table S2. Under ambient pressure and temperature conditions, the measured V_0 values of garnet,

205 omphacite, and epidote are 1566.05(25) Å^3, V_0 = 423.48(24) Å^3, and V_0 = 461.57(23) Å^3,

206 respectively. The fitting parameters under high-pressure and room-temperature yield K_{T0} = 170 (1)

207 GPa, K_{T0}' = 3.74 (22) for garnet, K_{T0} = 121 (2) GPa, K_{T0}' = 3.90 (35) for omphacite, and K_{T0} = 122

208 (1) GPa, K_{T0}' = 2.51 (16) for epidote, respectively.

209   To evaluate the quality of BM3-EoS fitting in this study, the relationship between the Eulerian

210 strain ($f_E = \left[(V_0/V)^{2/3} - 1 \right]$) and the normalized pressure ($F_E = P / \left[3f_E (2f_E + 1)^{5/2} \right]$) of

211 the main minerals for eclogite is plotted in Figure S3. Linear fitting of the three sets of data

212 exhibited a negative slope, indicating that the pressure derivative of the bulk modulus (K_{T0}') is less

213 than 4, which is consistent with our BM3-EoS fittings. The intercept value was obtained by

214 weighted linear regression of the data points, showing that $F_E(0)$=171 (2) GPa for garnet,

215 $F_E(0)$=123 (2) for omphacite, and $F_E(0)$=122 (1) for epidote, respectively. The results are

216 consistent with the fitted isothermal bulk modulus (K_{T0} = 170 (1) GPa for garnet, K_{T0} = 121 (2)

217 GPa for omphacite, and K_{T0} = 122 (1) GPa for epidote, respectively) within the error range.

218 Accordingly, the K_{T0} and K_{T0}' obtained by the BM3-EoS fitting are reasonable. Using the V_0 fixed

219 at ambient conditions to fit third-order Birch-Murnaghan and Holland-Powell thermal-pressure

220 EoS (BM3-HP-EoS), the available EoS parameters, K_{T0} = 170 (1) GPa, K_{T0}' = 3.82 (14), and α_0 =

221 2.71 (5) $\times 10^{-5}$ K^{-1} for garnet; K_{T0} = 121 (3) GPa, K_{T0}' = 3.97 (34), and α_0 = 3.73 (20) $\times 10^{-5}$ K^{-1} for

222 omphacite; and K_{T0} = 124 (2) GPa, K_{T0}' = 2.04 (15), and α_0 = 3.04 (13) $\times 10^{-5}$ K^{-1} for epidote are

223 derived. The *P-V-T* data fitted through the BM3-HP-EoS model are shown in Figure 3.

224 **4.2 Comparison with previous studies**

225 **4.2.1 Garnet**

226 The thermal EoS parameters of garnet are obtained by fitting the *P-V-T* data to the BM3-EoS. We

227 compare our results with those of previous studies (Arimoto et al., 2015; Gréaux and Yamada,

228 2014; Lu et al., 2013; Milani et al., 2015, 2017; Xu et al., 2019; Zou et al., 2012). The K_{T0} of end-

229 member garnet, pyrope, almandine, grossular, and spessartine crystals is between 158 and 179

230 GPa, and the bulk modulus of almandine is the largest among the above (Table S3). From Table

231 S3, it can be seen that bulk modulus of powder XRD (Arimoto et al., 2015; Gréaux and Yamada,

232 2014; Pavese et al., 2001; Zou et al., 2012) are larger than those of single-crystal XRD (Milani et

233 al., 2015, 2017) with the same composition. The K_{T0} of solid solution garnets (Beyer et al., 2021;

234 Jiang et al., 2004; Lu et al., 2013; Xu et al., 2019) is also between 158 and 179 GPa mentioned

235 above and will be affected by the end-member components. The K_{T0}=170 (1) GPa in this study is

236 reasonable within this range. The obtained K_{T0}' =3.82 (14) in this study is slightly lower than that

237 in previous studies. The Eulerian strain and the normalized pressure of the garnet shown in Figure

238 S3(a) exhibit a negative slope, which indicating K_{T0}' is less than 4. Moreover, compared with the

239 previous results, the obtained value of K_{T0}' in this study is within the error range (Supporting

240 Information Text S1). However, there is no obvious correlation between the fitted K_{T0} and K_{T0}' for

241 minerals of different compositions (Fig. S4); hence, the K_{T0} may not be precise when K_{T0}' is fixed.

242 For the α_0, the andradite has the largest value (3.16 (2)$\times 10^{-5}$ K^{-1}), and the grossular has the

243   smallest value (2.09 (2)$\times 10^{-5}$ K^{-1}) among the end-member garnets. The thermal expansion

244   coefficient of Prp$_{21}$Alm$_{47}$Grs$_{31}$Sps$_1$ (2.71 (5)$\times 10^{-5}$ K^{-1}) in this study is comparable with previous

245   studies, but the influence of composition still needs to be considered.

246   **4.2.2 Omphacite**

247   Many studies have focused on the thermoelastic properties of omphacite (Hao et al., 2019;

248   Nishihara et al., 2003; Pandolfo et al., 2012b, 2012a; Xu et al., 2019; Zhang et al., 2016) (Table

249   S3). Most of the results are obtained by the single-crystal XRD method, except for the result of

250   Nishihara et al. (2003), which was obtained from powder XRD. K_{T0}' shows a higher value of 6.9

251   (12) in the study of Nishihara et al. (2003), while in others, K_{T0}' is between 4 and 5.7, and the

252   result of K_{T0}' (3.97) in this study is slightly lower than the above values. Additionally, according to

253   the results shown in Table S3, the bulk moduli of omphacite are in the range of 115-123 GPa. In

254   the study of Xu et al. (2019), an increase in the iron content would decrease K_{T0}, and they also

255   discussed the reasons for the discrepancy in K_{T0} in detail, such as the effective ionic radius,

256   pressure transmitting medium, and experimental pressure range. Comparing our results with Xu et

257   al. (2019), we conclude that the incorporation of Fe would reduce the bulk modulus. However,

258   except for Fe content, there does not seem to be a significant correlation between the other

259   components and the bulk modulus of omphacite. The α_0 of the Di-Jd solid solution is similar (2.64

260   (2) $\times 10^{-5}$ K^{-1}-2.8 (3)$\times 10^{-5}$ K^{-1}) but less than that of Quad$_{48}$Jd$_{45}$Ae$_7$ (3.73 (20) $\times 10^{-5}$ K^{-1}) and

261   Quad$_{53}$Jd$_{27}$Ae$_{20}$ (3.4 (4)$\times 10^{-5}$ K^{-1}). It may be inferred that the Ae contents affect thermal expansion.

262   **4.2.3 Epidote**

263   The thermal EoS parameters of epidote in this study are compared with those reported in previous

264   studies (Fan et al., 2014; Gatta et al., 2011; Holland et al., 1996; Li et al., 2020; Qin et al., 2016)

265 (Table S3). Although the bulk modulus appears to be related to the Fe^{3+} content, it does not show a

266 good correlation. Increasing the content of Fe^{3+} can enhance the bulk modulus, but the result in

267 Holland et al. (1996) shows an abnormally large value of 162 (4) GPa, which is much higher than

268 the 111-133 GPa resulting from other studies. This may be attributed to the fixed K_{T0}' at 4 and

269 powder XRD methods used in the study of Holland et al. (1996). Furthermore, the K_{T0}' obtained

270 from powder XRD (Fan et al., 2014; Gatta et al., 2011) is also larger than that from single-crystal

271 XRD (Qin et al., 2016). The possible reasons for these discrepancies are complicated. Li et al.

272 (2020) conducted a detailed study on this topic. Previous studies on α_0 and $(\partial K_T/\partial T)_P$ of epidote

273 are limited. The α_0 (3.04 (13) $\times 10^{-5}$ K^{-1}) in this study is lower than that of Gatta et al. (2011) (5.1

274 (2) $\times 10^{-5}$ K^{-1}) and Li et al. (2020) (3.8 (5) $\times 10^{-5}$ K^{-1}).

275

276 **5   Implications**

277 In the Himalayan-Tibetan system, lithospheric removal is proposed to occur in either the breakoff

278 of the subducted slab of the Indian continental lithosphere (Chung et al., 2005; Turner et al., 1993)

279 or convective removal of the thickened lower part of the lithosphere (Miller et al., 1999). The

280 metamorphic eclogitization taking place in the subducted slab and the lowermost crust has been

281 deduced as the possible cause of subducted slab break-off and the convective removal of the lower

282 crust (Krystopowicz and Currie, 2013). Increased density in the eclogitized subducted slab and the

283 lower crust will promote the above two lithospheric removal modes if the lower crust is weak

284 enough for the negative buoyancy of the mantle lithosphere to be detached. Therefore, to better

285 consider the role of eclogite density variations in the process of lithospheric removal, we model

286 the density of minerals and eclogite aggregates along with the geotherms of Tibet and discuss the

287   effects of the degree of eclogitization on lithospheric removal.

288   The eclogite chemical data collected in Tibet and examined in our study come from a great

289   number of eclogite samples collected in previous studies (e.g. Chan et al., 2009; Liu et al., 2019;

290   Yang et al., 2009; Zhai et al., 2011a). The eclogite samples consist of garnet, omphacite, epidote,

291   amphibole, zoisite, symplectite along with minor phengite, quartz, rutile, and rare apatite, ilmenite,

292   and titanite as accessory minerals. Since the eclogite samples have suffered retrograde

293   metamorphism, we assume that is largely composed of garnet and omphacite plus slight epidote

294   before retrograde metamorphism. The accessory phases observed in natural eclogite are excluded

295   because of their minimal abundance of less than 5%. Based on the mineral composition data of

296   exposed eclogite in Tibet (Fig. S6) (e.g. Cheng et al., 2015; Dong et al., 2018; Huang et al., 2015;

297   Jin et al., 2019; Li et al., 2017; Zhai et al., 2011b, 2011a), the components of eclogite are 50

298   vol. % garnet + 45 vol. % omphacite + 5 vol. % epidote (parameterized as a value out of 100)

299   using the normal distribution.

300   We take into account two different delamination modes, namely, delamination caused by the

301   separation of the Neo-Tethyan slab (detachment of the subducted Neo-Tethyan oceanic slab) in the

302   Paleozoic and convective removal of the lower crust of the subducted Indian continent beneath the

303   Lhasa terrane during the Cenozoic. The temperature and pressure conditions of exposed eclogites

304   in the Paleozoic and Cenozoic are somewhat consistent with the geothermal lines provided by

305   previous studies (Fig. S7). The two different delamination modes reflect relatively cold geotherms

306   and hot geotherms, respectively. Therefore, these geothermal lines are used in our models. The

307   thermal EoS parameters of eclogitic garnet, omphacite, and epidote are derived through the BM3-

308   HP-EoS shown in supporting information Table S2.

5.1 The density of main minerals for eclogite along the geothermal profile in Tibet

309

310 Tibetan eclogite is mainly composed of garnet, and omphacite, with a few epidotes. As shown in

311 Figure 2, the exposed minerals differ in composition. The specific composition of minerals

312 constrains the density. Therefore, we refer to the thermoelastic parameters of Xu et al. (2019) and

313 Nishihara et al. (2003) to depict the density distribution of different components (Fe content) of

314 garnet and omphacite under Tibetan geothermal lines, respectively. The corresponding

315 thermoelastic parameters can be seen in Table S3. The mineral compositions of previous studies

316 are within the range of the Tibetan constituents collected in this study (Fig. 2).

317 The density distribution of minerals along with relatively cold Tibetan geothermal conditions is

318 shown in Figure 4 (the results along with hot geotherms can be seen in supporting information Fig.

319 S8). The result clearly shows that the density of garnet is linked with the iron content. The density

320 of garnet ($Prp_{21}Alm_{47}Grs_{31}Sps_1$, with 47 mol. % almandine) in this study is higher than that of

321 low-Fe garnet ($Prp_{28}Alm_{38}Grs_{33}Sps_1$, with 38 mol. % almandine) (Xu et al., 2019) by 2.22% but

322 lower than that of high-Fe garnet ($Prp_{14}Alm_{62}Grs_{19}Adr_3Sps_2$, with 62 mol. % almandine) (Xu et al.,

323 2019) by 3.82% at ~80 km (Fig. 4a). With increasing depth, the density of high-Fe garnet

324 increases by a larger amplitude. This discrepancy may be caused by its smaller degree of thermal

325 expansion ($2.56 (44) \times 10^{-5}$ K^{-1}). Accordingly, the influence of pressure on the density is greater

326 than that of temperature, which leads to faster increases in density with depth. The density of

327 omphacite does not show obvious characteristics related to its composition. The density of

328 omphacite ($Quad_{48}Jd_{45}Ae_7$, with 7 mol. % aegirine) in this study is lower than that of high-Fe

329 omphacite ($Quad_{53}Jd_{27}Ae_{20}$, with 20 mol. % aegirine) (Xu et al., 2019), $Quad_{72}Jd_{28}$ (Nishihara et

330 al., 2003), and $Quad_{57}Jd_{42}Ae_1$ (with 1 mol. % aegirine) (Xu et al., 2019) by 1.95%, 1.47%, and

331 0.83%, respectively, at ~80 km (Fig. 4b). The presence of iron in certain quantities does increase

332 the density of omphacite, but the density of omphacite is also affected by other elements, such as

333 calcium and magnesium. Moreover, thermal EoS parameters are also of vital importance to

334 calculate the density. The relatively low thermal expansion of $Quad_{72}Jd_{28}$ (2.7 (3)$\times10^{-5}$ K^{-1}) and

335 $Quad_{57}Jd_{42}Ae_1$ (with 1 mol. % aegirine) (2.8 (3)$\times10^{-5}$ K^{-1}) may further enhance the increasing rate

336 of density with depth. It is worth noting that the densities of $Quad_{48}Jd_{45}Ae_7$ (with 7 mol. %

337 aegirine) in this study and $Quad_{57}Jd_{42}Ae_1$ (with 1 mol. % aegirine) of Xu et al. (2019) are the same

338 under ambient conditions but inconsistent under high-pressure and high-temperature conditions.

339 Therefore, the K_{T0} and K_{T0}' of the two omphacites are somewhat consistent with each other, while

340 the thermal expansion and $(\partial K_T/\partial T)_P$ are different. Collectively, the thermal EoS parameters are of

341 the essence in the derivation of the mineral density.

342 **5.2 The density of eclogite in Tibet**

343 Eclogitized crust and lithospheric mantle may be potential factors causing delamination (Faccenda

344 et al., 2009; Krystopowicz and Currie, 2013). The density of eclogite and peridotite can provide

345 new constraints to control the breakoff of the subducted slab and convective removal of the

346 lithosphere in the process of delamination. Therefore, we plot the density distribution of eclogite

347 with different garnet contents and peridotite along the Paleozoic and Cenozoic Tibetan geotherms,

348 as shown in Figure 5. In our model, the mineral composition of Tibetan eclogite is in the range of

349 40 vol. % garnet + 55 vol. % omphacite + 5 vol. % epidote to 60 vol. % garnet + 35 vol. %

350 omphacite + 5 vol. % epidote based on the exposed eclogite in Tibet (the composition of epidote is

351 only 5 vol. % default due to its low content in this study). The composition of surrounding

352 peridotite consists of 70 vol. % olivine + 25 vol. % orthopyroxene + 3 vol. % clinopyroxene + 2

353   vol. % spinel (Yang et al., 2019; Zhao et al., 2021). The densities of eclogite and peridotite

354   aggregates are obtained considering their arithmetic mean. The densities of each mineral under

355   specific temperature and pressure conditions are derived by the following formula:

356
$$\rho(T,P) = \frac{V(T,0)}{V(T,P)} \times \frac{Z \times M}{N_a \times V_0} \qquad (4)$$

357   where V_0 is the reference unit cell volume at ambient conditions, M is molecular weight, Z is the

358   number of formula units in the unit cell and N_a is the Avogadro number.

359   Most changes in the deep conditions of the Earth are progressing slowly, so there is adequate

360   time for recrystallization to relieve the maximum stress point (Robertson, 1988; Skinner, 1966).

361   Here, we assume that the elastic-plastic interaction among different minerals and possible

362   deviations from hydrostatic conditions are ignored and the density of the eclogite aggregate can be

363   obtained by the arithmetic mean as follows:

364
$$\overline{\rho} = \sum \lambda_i \rho_i(T,P) \qquad (5)$$

365   where the subscript i denotes the ith mineral of the upper mantle, and λ is the volume proportion

366   of each mineral.

367   The densities of Tibetan eclogite (with the garnet composition of $Prp_{21}Alm_{47}Grs_{31}Sps_1$, the

368   omphacite   composition   of $Quad_{48}Jd_{45}Ae_7$,   and   the   epidote   composition   of

369   $Ca_{2.02}Fe_{0.75}Al_{2.32}Si_{0.16}(SiO_4)(Si_2O_7)O(OH))$ and peridotite (with the olivine composition of

370   $Fo_{89.9}Fa_{10.1}$, the orthopyroxene composition of $En_{89.6}Fs_{9.7}Wo_{0.7}$, the clinopyroxene composition of

371   $Quad_{88.5}Jd_{11.5}$,   and   the   spinel   composition   of

372   $(Mg_{0.790}Fe_{0.204}Ni_{0.005}Ti_{0.001})_{1.000}(Al_{0.821}Cr_{0.158}Fe_{0.021})_{2.002}O_4)$ in this study along the Paleozoic

373   geothermal line are shown in Figure 5a. The results show that the increase in garnet has a

374   profound influence on the density of eclogite. For every 10% increase in garnet, the density of

375   eclogite increases by ~1.7%. The garnet content in Tibetan eclogite is estimated to be 40 vol. %-60

376   vol. % (Fig. S6). The densities of this part of eclogite are 3.54-3.66 g/cm^3, which is approximately

377   7.4%-11.2% more than that of peridotite (3.29 g/cm^3) at ~80 km. The density difference between

378   eclogite and peridotite is 0.24 g/cm^3-0.37 g/cm^3 (Fig. 5b). At the same time, we also consider the

379   density of eclogite aggregates without epidote (Fig. S6). The results show that 5 vol. % epidote

380   has little effect on the density of eclogite, especially eclogite with garnet contents of 50 vol. %-60

381   vol. % (Fig. S9). To account for the role of iron, the density distributions of high-Fe

382   ($Prp_{14}Alm_{62}Grs_{19}Adr_3Sps_2$ and $Quad_{53}Jd_{27}Ae_{20}$ and low-Fe eclogite ($Prp_{28}Alm_{38}Grs_{33}Sps_1$ and

383    $Quad_{57}Jd_{42}Ae_1$) are plotted to better constrain the range of eclogite density (Fig. S10) (Xu et al.,

384   2019). For high-Fe and low-Fe eclogites, the densities of eclogite increase by ~1.9% and ~1.4%

385   for each 10% increase in garnet, respectively. The densities of eclogite are 3.64 g/cm^3-3.78 g/cm^3

386   for high-Fe content and 3.53 g/cm^3-3.63 g/cm^3 for low-Fe content at ~80 km. Furthermore, the

387   densities of high-Fe and low-Fe eclogites are 10.6%-14.9% and 7.2%-10.3% higher than the

388   surrounding peridotite, respectively. For a more straightforward comparison, taking eclogite

389   containing 50 vol. % garnet as an example (Fig. S11), the densities of high-Fe eclogite, low-Fe

390   eclogite, and Tibetan eclogite at ~80 km are 3.71 g/cm^3, 3.58 g/cm^3, and 3.61 g/cm^3, respectively.

391   An increase in the iron content can substantially increase the density of eclogite, although it will

392   be constrained by the thermal EoS parameters of minerals.

393   Similarly, we also discuss the density profile along the Cenozoic geothermal line, which can be

394   seen in supporting information Text S2. In any case, the density difference caused by eclogite may

395   be one of the prominent factors instigating the delamination process.

396   **5.3 Influence of the degree of eclogitization on the density of the subducted slab**

397   Eclogite in the mantle, which is believed to be 5%-10% denser than peridotite (Garber et al.,

398   2018), is responsible for the excess compositional density. Furthermore, some calculations

399   propose that the degree of eclogitization of the subducted slab is a key factor in the delamination

400   process (Matchette-Downes et al., 2019). To investigate the influence of the degree of

401   eclogitization in the delamination process, we plot the density variations with different mineral

402   compositions under different degrees of eclogitization (Fig. 6). We consider eclogitization in the

403   lithospheric mantle of the subducted slab, here the degree of eclogitization refers to the amount of

404   eclogite in the lithospheric mantle. In our preferred model, the 7-km thick subducted oceanic crust

405   becomes eclogite, while the lithospheric mantle constrains a different amount of eclogite. Since

406   the subducted Indian oceanic slab might be fragmented into several pieces, the longitudinal size of

407   the fractured slab is postulated to be 60 km (Peng et al., 2016). Our estimated average density of

408   the fragmented slab with various degrees of eclogitization is shown in Figure 6a. The results

409   clearly show that the density increases monotonically with the garnet content and the degree of

410   eclogitization. The garnet content is of profound importance to the density of eclogite. The higher

411   the proportion of garnet is, the greater the density increases with increasing degrees of

412   eclogitization. The garnet content in Tibetan eclogite is estimated to be between 40-60 vol. %.

413   Taking garnet with an average volume percentage of 50 vol. % in Tibetan eclogite as an example,

414   the density of eclogitized subducted slabs ranges from 3.35 g/cm^3 with 10% eclogitization to 3.61

415   g/cm^3 with 100 vol. % eclogitization. For a garnet content of 50 vol.%, the density increases by

416   0.029 g/cm^3 per 10 vol. % increase in the degree of eclogitization. The density will increase with

417   increasing garnet contents, from 0.006 g/cm^3 for 10 vol. % to 0.051 g/cm^3 for 90 vol. %. The

418   densities of high-Fe and low-Fe eclogitized fragmented slabs are also shown in Figure S12. The

419   high-Fe content shows that the density variation increases with the degree of eclogitization from

420   0.007 g/cm^3 for 10 vol. % to 0.064 g/cm^3 for 90 vol. % garnet, while the low-Fe content shows a

421   density change from 0.004 g/cm^3 for 10 vol. % garnet to 0.045 g/cm^3 for 90 vol. % garnet.

422   **5.4 Delamination in Tibet**

423   The development of delamination is associated with the instability of the lower crust and the

424   mantle lithosphere. The eclogitization of the subducted slab and lower crust plays a vital role in

425   the process of delamination due to the high density of eclogite, which makes the formation denser

426   than the surrounding mantle lithosphere and provides critical negative buoyancy (Göğüş and Ueda,

427   2018; Krystopowicz and Currie, 2013). The densities of the eclogitic lower crust and mantle

428   lithosphere during slab subduction and convective removal are sufficiently higher than that of the

429   asthenosphere and are good candidates for the initiation of destabilization.

430   **5.4.1 Subducted slab breakoff**

431   A series of collisional breakoff events is proposed to have occurred throughout 60-45 Ma in Tibet

432   (Chung et al., 2005, 2009; Ma et al., 2014; Zhu et al., 2015). The formation of eclogite

433   presumably kick-starts slab breakoff during the subduction of the Indian oceanic plate underthrust

434   below the southern margin of Tibet. The subducted Indian oceanic slab fragmented into several

435   pieces, due to what has been identified as a high-velocity anomaly (Peng et al., 2016; Shi et al.,

436   2020b). The seismological evidence of high density (Hetényi et al., 2007), high V_P (Schulte-

437   Pelkum et al., 2005), and low longitudinal/transverse (V_P/V_S) ratios (Wittlinger et al., 2009) further

438   confirms that there may be variable degrees of eclogitization beneath Tibet. Figure 6 shows the

439   density profile of subducted slabs with different garnet compositions, different degrees of

440   eclogitization, and variable densities compared with the surrounding peridotite. An increasing

441 degree of eclogitization and an enhanced garnet content in eclogite increases the density difference

442 between the slab and the surrounding peridotite. Previous studies have made preliminary estimates

443 of the average density from the isostatic balance and geoid anomalies and postulated that the

444 density excess could be between 0-0.19 g/cm^3 (Matchette-Downes et al., 2019). For Tibetan

445 eclogite containing 40 vol. %-60 vol. % garnet, if the lithospheric mantle is a mixture of peridotite

446 and eclogite with a density anomaly of 0.19 g/cm^3, our model requires a range of 44%-70%

447 degrees of eclogitization. If the eclogite is high-Fe, only a 30%-48% degree of eclogitization is

448 needed to produce the density difference (Fig. S12), while an eclogitization degree is in the range

449 of 49%-74% is needed for the low-Fe eclogite. However, some seismological data show that the

450 crust or lithospheric mantle being only ~30% eclogitized might cause gravitational instability in

451 Tibet (Matchette-Downes et al., 2019; Shi et al., 2020a), which is lower than our estimation. Our

452 results clearly show that density excess is closely linked with garnet content and eclogitization

453 degree. If eclogite has a high garnet content, a relatively low degree of eclogitization could

454 instigate the delamination of slab breakoff.

455 On the other hand, the presence of a weak lower crust and a vertical conduit to accommodate

456 asthenosphere influx is also necessary for the delamination process. The weak layer between the

457 residual crustal and downward peeling lithosphere layer (and/or lower crust) (Göğüş and Ueda,

458 2018) could promote the initiation and propagation of delamination. Therefore, very high

459 temperatures and relatively low lower-crustal viscosities are also other controlling factors of

460 delamination (Göğüş and Pysklywec, 2008; Morency, 2004). Here, we assume that the length of

461 the fractured slab is 60 km, which drops 80 km over 45 Ma and that the viscosity of the

462 asthenosphere is $5*10^{20}$ Pa·S (Wang et al., 2019). By using Stokes' Law (Supporting Information

463   Text S3), ignoring the thermal disturbance, and assuming the most ideal conditions, the density

464   difference caused by eclogite needs to be at least 0.15 g/cm^3 to produce such delamination. The

465   result is close to those discussed above in gravity anomalies.

466   In particular, the presence of eclogite with a greater abundance of garnet, a higher-Fe content,

467   and a greater degree of eclogitization would instigate the delamination process of slab breakoff.

468   **5.4.2 Removal of the eclogitized lower crust**

469   The thickened lower crust undergoes "convective removal" due to gravitational instability, which

470   is another type of delamination that occurred in Tibet from 25 Ma to 0 Ma (Chung et al., 2005;

471   Nomade et al., 2004). The convective removal of the lithosphere during delamination corresponds

472   to higher temperature conditions (Craig et al., 2020). In this circumstance, the density of Tibetan

473   eclogite is 6.9%-10.8% denser than the surrounding peridotite at ~60 km (Fig. 5b), which is

474   analogous to the results in the case of subducted slab detachment. This result is also in ample

475   agreement with the result obtained by Garber et al. (2018), which noted that eclogite is 5%-10%

476   denser than peridotite. The density difference between eclogite and peridotite is 0.22 g/cm^3-0.35

477   g/cm^3 with 40 vol. %-60 vol. % garnet in Tibet (Fig. 5d). During this stage, it is believed that

478   delamination of the thickened, eclogitized lower crust has occurred. Similarly, Stokes' law can be

479   used considering ideal conditions without any thermal disturbance. If the falling block is assumed

480   to be approximately 30 km in the longitudinal direction and the viscosity of the asthenosphere is

481   $5*10^{20}$ Pa·S, the falling block can drop by 70-110 km within 25 Ma. For eclogite with a high-Fe

482   content, a density difference of 0.35 g/cm^3-0.50 g/cm^3 makes the fragmented block capable of

483   falling 105-155 km, while the density difference of 0.24 g/cm^3-0.33 g/cm^3 with a low-Fe content

484   makes the block able to fall 75-102 km (Fig. S13). The fragmented block with a high-Fe content

485 can fall a larger distance at the same time, indicating that the high-Fe content is more likely to

486 promote the occurrence of delamination. This result is consistent with the high-velocity

487 anomalous blocks identified at 100-200 km by seismic tomography (Peng et al., 2016; Shi et al.,

488 2016, 2020a).

489 In summary, density contrasts can provide a stimulus for the initiation of instability. It is accepted

490 that eclogite with a high garnet content and a high Fe content and a high proportion of eclogite in

491 the lithospheric mantle may have strongly promoted delamination during the process of India-Asia

492 collision from the perspective of density.

493

494 **6. Conclusion**

495 The *P-V-T* EoS of the main minerals of eclogite is combined with its mineral composition

496 and the geothermal line to derive the density of Tibetan eclogite in this study. We offer a new

497 perspective by obtaining the thermal EoS for the main minerals of eclogite in a single experiment.

498 The thermal EoS parameters of the main minerals of eclogite are derived by fitting the *P-V-T* data

499 to the HT-BM-EoS. The density of minerals along the Tibetan geotherm shows that the density is

500 closely related to its composition and thermal EoS parameters. Increasing iron contents increase

501 the density of minerals, but if the molecular masses of two minerals are similar, the thermal EoS

502 parameters play a pivotal role. The garnet content profoundly increases the density of eclogite. For

503 every 10 vol. % increase in garnet, the density of eclogite increases by approximately 1.7%. The

504 density of Tibetan eclogite is approximately 7-11% denser than that of the surrounding peridotite.

505 An increasing proportion of garnet, Fe content, and degree of eclogitization enhance the density

506 difference to facilitate the delamination process. For Tibetan eclogite containing 40-60 vol. %

507 garnet, 44-70% degrees of eclogitization can produce the same density difference as obtained by

508 the isostatic balance and the geoid anomaly. According to a rough calculation, the fragmented

509 block will fall 70-155 km. A high-Fe content is more likely to promote delamination. Eclogite is a

510 good candidate for the initiation of instability and may be more susceptible to inducing the

511 breakoff of the subducted slab or the gravitational removal of the lower crust during the process of

512 the India-Asia collision.

513

514 **Data availability**

515 All the data presented in this paper are available upon request.

516

517 **Author contributions**

518 All authors contributed to the preparation and revision of the manuscript. Z. Ye: Data curation,

519 Investigation, Formal analysis, Writing-original draft, Writing-review & editing. D. Fan:

520 Investigation, Conceptualization, Supervision, Methodology, Funding acquisition, Writing-review

521 & editing. B. Li: Data curation, Writing-review & editing. Q. Tang: Software, Validation, Writing-

522 review & editing. J. Xu: Investigation, Supervision, Writing-review & editing. D. Zhang: Formal

523 analysis, Writing-review & editing. W. Zhou: Investigation, Conceptualization, Supervision,

524 Writing-review & editing.

525

526 **Competing interests**

527 The authors declare that they have no conflict of interest.

528

Disclaimer

Acknowledgments

This project was funded by the National Natural Science Foundation of China (Grant Nos. 42172048, U2032118 and 41802043), the Youth Innovation Promotion Association CAS (Dawei Fan, 2018434), the Chinese Academy of Sciences "Light of West China" Program (2019), the Guizhou Provincial Science and Technology Projects (QKHJC-ZK[2021]ZD042), and the Innovation and Entrepreneurship Funding of High-Level Overseas Talents of Guizhou Province (Dawei Fan, [2019] 10).

Supplementary Information. The supplementary information describes the density profile of garnet at high temperature, density profile along Cenozoic geothermal line, data of unit-cell parameters of eclogite minerals, thermal EoS parameters of this study and previous researches, figures of Eulerian finite stain-normalized pressure (F_E -f_E), isothermal bulk modulus (K_{T0}) and its pressure derivative (K_{T0}') plot of garnet and omphacite, normal distribution of eclogite minerals, density evolution of minerals, and density profile of different Fe-content eclogite.

References:

Angel, R. J., Alvaro, M. and Gonzalez-Platas, J.: EosFit7c and a Fortran module (library) for equation of state calculations, Zeitschrift für Krist. - Cryst. Mater., 229(5), doi:10.1515/zkri-2013-1711, 2014.

Angel, R. J., Alvaro, M. and Nestola, F.: 40 years of mineral elasticity: a critical review and a new

552   parameterisation of equations of state for mantle olivines and diamond inclusions, Phys. Chem. Miner.,

553   45(2), 95–113, doi:10.1007/s00269-017-0900-7, 2018.

554   Arimoto, T., Gréaux, S., Irifune, T., Zhou, C. and Higo, Y.: Sound velocities of $Fe_3Al_2Si_3O_{12}$

555   almandine up to 19 GPa and 1700 K, Phys. Earth Planet. Inter., 246, 1–8,

556   doi:10.1016/j.pepi.2015.06.004, 2015.

557   Beyer, C., Kurnosov, A. V., Ballaran, T. B. and Frost, D. J.: High-pressure and high-temperature

558   single-crystal X-ray diffraction of complex garnet solid solutions up to 16 GPa and 823 K, Phys. Chem.

559   Miner., 48(4), 17, doi:10.1007/s00269-021-01139-5, 2021.

560   Birch, F.: Finite Elastic Strain of Cubic Crystals, Phys. Rev., 71(11), 809–824,

561   doi:10.1103/PhysRev.71.809, 1947.

562   Birch, F.: Finite strain isotherm and velocities for single-crystal and polycrystalline NaCl at high

563   pressures and 300 K, J. Geophys. Res., 83(B3), 1257, doi:10.1029/JB083iB03p01257, 1978.

564   Bird, P.: Initiation of intracontinental subduction in the Himalaya, J. Geophys. Res. Solid Earth,

565   83(B10), 4975–4987, doi:10.1029/JB083iB10p04975, 1978.

566   Bird, P.: Continental delamination and the Colorado Plateau, J. Geophys. Res. Solid Earth, 84(B13),

567   7561–7571, doi:10.1029/JB084iB13p07561, 1979.

568   Chan, G. H. N., Waters, D. J., Searle, M. P., Aitchison, J. C., Horstwood, M. S. A., Crowley, Q., Lo, C.

569   H. and Chan, J. S. L.: Probing the basement of southern Tibet: evidence from crustal xenoliths

570   entrained in a Miocene ultrapotassic dyke, J. Geol. Soc. London., 166(1), 45–52, doi:10.1144/0016-

571   76492007-145, 2009.

572   Chen, W. and Tenzer, R.: The application of a gravimetric forward modelling of the lithospheric

573   structure for an estimate of the average density of the upper asthenosphere, Geod. Geodyn., 10(4), 265–

574   275, doi:10.1016/j.geog.2019.04.003, 2019.

575   Cheng, H., Zhang, C., Vervoort, J. D., Lu, H., Wang, C. and Cao, D.: Zircon U–Pb and garnet Lu–Hf

576   geochronology of eclogites from the Lhasa Block, Tibet, Lithos, 155, 341–359,

577   doi:10.1016/j.lithos.2012.09.011, 2012.

578   Cheng, H., Liu, Y., Vervoort, J. D. and Lu, H.: Combined U-Pb, Lu-Hf, Sm-Nd and Ar-Ar

579   multichronometric dating on the Bailang eclogite constrains the closure timing of the Paleo-Tethys

580   Ocean in the Lhasa terrane, Tibet, Gondwana Res., 28(4), 1482–1499, doi:10.1016/j.gr.2014.09.017,

581   2015.

582   Chung, S.-L., Chu, M.-F., Zhang, Y., Xie, Y., Lo, C.-H., Lee, T.-Y., Lan, C.-Y., Li, X., Zhang, Q. and

583   Wang, Y.: Tibetan tectonic evolution inferred from spatial and temporal variations in post-collisional

584   magmatism, Earth-Science Rev., 68(3–4), 173–196, doi:10.1016/j.earscirev.2004.05.001, 2005.

585   Chung, S.-L., Chu, M.-F., Ji, J., O'Reilly, S. Y., Pearson, N. J., Liu, D., Lee, T.-Y. and Lo, C.-H.: The

586   nature and timing of crustal thickening in Southern Tibet: Geochemical and zircon Hf isotopic

587   constraints from postcollisional adakites, Tectonophysics, 477(1–2), 36–48,

588   doi:10.1016/j.tecto.2009.08.008, 2009.

589   Conrad, C. P. and Molnar, P.: Convective instability of a boundary layer with temperature-and strain-

590   rate-dependent viscosity in terms of "available buoyancy," Geophys. J. Int., 139(1), 51–68,

591   doi:10.1046/j.1365-246X.1999.00896.x, 1999.

592   Corrie, S. L., Kohn, M. J. and Vervoort, J. D.: Young eclogite from the Greater Himalayan Sequence,

593   Arun Valley, eastern Nepal: P–T–t path and tectonic implications, Earth Planet. Sci. Lett., 289(3–4),

594   406–416, doi:10.1016/j.epsl.2009.11.029, 2010.

595   Craig, T. J., Kelemen, P. B., Hacker, B. R. and Copley, A.: Reconciling Geophysical and Petrological

596   Estimates of the Thermal Structure of Southern Tibet, Geochemistry, Geophys. Geosystems, 21(8),

597   doi:10.1029/2019GC008837, 2020.

598   DeCelles, P. G., Robinson, D. M. and Zandt, G.: Implications of shortening in the Himalayan fold-

599   thrust belt for uplift of the Tibetan Plateau, Tectonics, 21(6), 12-1-12–25, doi:10.1029/2001TC001322,

600   2002.

601   Dera, P., Zhuravlev, K., Prakapenka, V., Rivers, M. L., Finkelstein, G. J., Grubor-Urosevic, O.,

602   Tschauner, O., Clark, S. M. and Downs, R. T.: High pressure single-crystal micro X-ray diffraction

603   analysis with GSE_ADA/RSV software, High Press. Res., 33(3), 466–484,

604   doi:10.1080/08957959.2013.806504, 2013.

605   Dong, Y.-L., Wang, B.-D., Zhao, W.-X., Yang, T.-N. and Xu, J.-F.: Discovery of eclogite in the

606   Bangong Co–Nujiang ophiolitic mélange, central Tibet, and tectonic implications, Gondwana Res., 35,

607   115–123, doi:10.1016/j.gr.2016.03.010, 2016.

608   Dong, Y., Xie, C., Yu, Y., Wang, B., Li, L. and Zeng, X.: The discovery of Longyasongduo eclogite

609   from Gongbujiangda County, Tibet, and its significance., Geol. Bull. Of China, 37(8), 2018.

610   Ehlers, T. A. and Poulsen, C. J.: Influence of Andean uplift on climate and paleoaltimetry estimates,

611   Earth Planet. Sci. Lett., 281(3–4), 238–248, doi:10.1016/j.epsl.2009.02.026, 2009.

612   Faccenda, M., Minelli, G. and Gerya, T. V.: Coupled and decoupled regimes of continental collision:

613   Numerical modeling, Earth Planet. Sci. Lett., 278(3–4), 337–349, doi:10.1016/j.epsl.2008.12.021, 2009.

614   Faccincani, L., Faccini, B., Casetta, F., Mazzucchelli, M., Nestola, F. and Coltorti, M.: EoS of mantle

615   minerals coupled with composition and thermal state of the lithosphere: Inferring the density structure

616   of peridotitic systems, Lithos, 404–405(September), 106483, doi:10.1016/j.lithos.2021.106483, 2021.

617   Fan, D., Xu, J., Wei, S., Chen, Z. and Xie, H.: In-situ high-pressure synchrotron X-ray diffraction of

natural epidote, Chin. J. High Press. Phys., 28, 257–261, doi:10.11858/gywlxb.2014.03.001, 2014.

Fei, Y., Ricolleau, A., Frank, M., Mibe, K., Shen, G. and Prakapenka, V.: Toward an internally

consistent pressure scale, Proc. Natl. Acad. Sci., 104(22), 9182–9186, doi:10.1073/pnas.0609013104,

2007.

Finkelstein, G. J., Jackson, J. M., Sturhahn, W., Zhang, D., Alp, E. E. and Toellner, T. S.: Single-

crystal equations of state of magnesiowüstite at high pressures, Am. Mineral., 102(8), 1709–1717,

doi:10.2138/am-2017-5966, 2017.

Garber, J. M., Maurya, S., Hernandez, J., Duncan, M. S., Zeng, L., Zhang, H. L., Faul, U., McCammon,

C., Montagner, J., Moresi, L., Romanowicz, B. A., Rudnick, R. L. and Stixrude, L.: Multidisciplinary

Constraints on the Abundance of Diamond and Eclogite in the Cratonic Lithosphere, Geochemistry,

Geophys. Geosystems, 19(7), 2062–2086, doi:10.1029/2018GC007534, 2018.

Gatta, G. D., Merlini, M., Lee, Y. and Poli, S.: Behavior of epidote at high pressure and high

temperature: a powder diffraction study up to 10 GPa and 1200 K, Phys. Chem. Miner., 38(6), 419–428,

doi:10.1007/s00269-010-0415-y, 2011.

Göğüş, O. H. and Pysklywec, R. N.: Near-surface diagnostics of dripping or delaminating lithosphere, J.

Geophys. Res., 113(B11), B11404, doi:10.1029/2007JB005123, 2008.

Göğüş, O. H. and Ueda, K.: Peeling back the lithosphere: Controlling parameters, surface expressions

and the future directions in delamination modeling, J. Geodyn., 117(March), 21–40,

doi:10.1016/j.jog.2018.03.003, 2018.

Gottschalk, M.: Thermodynamic Properties of Zoisite, Clinozoisite and Epidote, Rev. Mineral.

Geochemistry, 56(1), 83–124, doi:10.2138/gsrmg.56.1.83, 2004.

Gréaux, S. and Yamada, A.: P-V-T equation of state of $Mn_3Al_2Si_3O_{12}$ spessartine garnet, Phys. Chem.

640   Miner., 41(2), 141–149, doi:10.1007/s00269-013-0632-2, 2014.

641   Guillot, S., Mahéo, G., de Sigoyer, J., Hattori, K. H. and Pêcher, A.: Tethyan and Indian subduction

642   viewed from the Himalayan high- to ultrahigh-pressure metamorphic rocks, Tectonophysics, 451(1–4),

643   225–241, doi:10.1016/j.tecto.2007.11.059, 2008.

644   Hacker, B. R.: Hot and Dry Deep Crustal Xenoliths from Tibet, Science (80)., 287(5462), 2463–2466,

645   doi:10.1126/science.287.5462.2463, 2000.

646   Hao, M., Zhang, J. S., Pierotti, C. E., Ren, Z. and Zhang, D.: High-Pressure Single-Crystal Elasticity

647   and Thermal Equation of State of Omphacite and Their Implications for the Seismic Properties of

648   Eclogite in the Earth's Interior, J. Geophys. Res. Solid Earth, 124(3), 2368–2377,

649   doi:10.1029/2018JB016964, 2019.

650   He, Y., Li, S., Hoefs, J., Huang, F., Liu, S.-A. and Hou, Z.: Post-collisional granitoids from the Dabie

651   orogen: New evidence for partial melting of a thickened continental crust, Geochim. Cosmochim. Acta,

652   75(13), 3815–3838, doi:10.1016/j.gca.2011.04.011, 2011.

653   Hetényi, G., Cattin, R., Brunet, F., Bollinger, L., Vergne, J., Nábělek, J. L. and Diament, M.: Density

654   distribution of the India plate beneath the Tibetan plateau: Geophysical and petrological constraints on

655   the kinetics of lower-crustal eclogitization, Earth Planet. Sci. Lett., 264(1–2), 226–244,

656   doi:10.1016/j.epsl.2007.09.036, 2007.

657   Hodges, K. V., Hurtado, J. M. and Whipple, K. X.: Southward extrusion of Tibetan crust and its effect

658   on Himalayan tectonics, Tectonics, 20(6), 799–809, doi:10.1029/2001TC001281, 2001.

659   Holland, T. J. B., Redfern, S. A. T. and Pawley, A. R.: Volume behavior of hydrous minerals at high

660   pressure and temperature; II, Compressibilities of lawsonite, zoisite, clinozoisite, and epidote, Am.

661   Mineral., 81(3–4), 341–348, doi:10.2138/am-1996-3-408, 1996.

662   Holland, T. J. B. and Powel, R.: An improved and extended internally consistent thermodynamic

663   dataset for phases of petrological interest, involving a new equation of state for solids, J. Metamorph.

664   Geol., 29(3), 333–383, doi:10.1111/j.1525-1314.2010.00923.x, 2011.

665   Houseman, G. and McKenzie, D. P.: Numerical experiments on the onset of convective instability in

666   the Earth's mantle, Geophys. J. Int., 68(1), 133–164, doi:10.1111/j.1365-246X.1982.tb06966.x, 1982.

667   Houseman, G. A., McKenzie, D. P. and Molnar, P.: Convective instability of a thickened boundary

668   layer and its relevance for the thermal evolution of continental convergent belts, J. Geophys. Res. Solid

669   Earth, 86(B7), 6115–6132, doi:10.1029/JB086iB07p06115, 1981.

670   Huang, J., Tian, Z. Z., Zhang, C., Yang, J. J. and Chen, M.: Metamorphic evolution of Sumdo eclogite

671   in Lhasa Block of the Tibetan Plateau: Phase equilibrium in NCKMnFMASHTO System, Geol. China,

672   42(5), 1559–1571, 2015.

673   Jiang, F., Speziale, S. and Duffy, T. S.: Single-crystal elasticity of grossular- and almandine-rich

674   garnets to 11 GPa by Brillouin scattering, J. Geophys. Res. Solid Earth, 109(B10),

675   doi:10.1029/2004JB003081, 2004.

676   Jin, X., Zhang, Y.-X., Zhou, X.-Y., Zhang, K.-J., Li, Z.-W., Khalid, S. Bin, Hu, J.-C., Lu, L. and Sun,

677   W.-D.: Protoliths and tectonic implications of the newly discovered Triassic Baqing eclogites, central

678   Tibet: Evidence from geochemistry, Sr Nd isotopes and geochronology, Gondwana Res., 69, 144–162,

679   doi:10.1016/j.gr.2018.12.011, 2019.

680   Klotz, S., Chervin, J.-C., Munsch, P. and Le Marchand, G.: Hydrostatic limits of 11 pressure

681   transmitting media, J. Phys. D. Appl. Phys., 42(7), 075413, doi:10.1088/0022-3727/42/7/075413, 2009.

682   Krystopowicz, N. J. and Currie, C. A.: Crustal eclogitization and lithosphere delamination in orogens,

683   Earth Planet. Sci. Lett., 361, 195–207, doi:10.1016/j.epsl.2012.09.056, 2013.

684   Levin, L. E.: Structure of the thermal lithosphere and asthenosphere beneath oceans and continents,

685   Geotectonics, 40(5), 357–366, doi:10.1134/S0016852106050037, 2006.

686   Li, B., Xu, J., Zhang, D., ZhilinYe, Huang, S., Fan, D., Zhou, W. and Xie, H.: Thermoelasticity and

687   stability of natural epidote at high pressure and high temperature: Implications for water transport

688   during cold slab subduction, Geosci. Front., (January), doi:10.1016/j.gsf.2020.05.022, 2020.

689   Li, C., van der Hilst, R. D., Meltzer, A. S. and Engdahl, E. R.: Subduction of the Indian lithosphere

690   beneath the Tibetan Plateau and Burma, Earth Planet. Sci. Lett., 274(1–2), 157–168,

691   doi:10.1016/j.epsl.2008.07.016, 2008.

692   Li, H. and Fang, J.: Crustal and upper mantle density structure beneath the qinghai-tibet plateau and

693   surrounding areas derived from EGM2008 geoid anomalies, ISPRS Int. J. Geo-Information, 6(1), 1–15,

694   doi:10.3390/ijgi6010004, 2017.

695   Li, J. X., Fan, W. M., Zhang, L. Y., Ding, L., Sun, Y. L., Peng, T. P., Cai, F. L., Guan, Q. Y. and Sein,

696   K.: Subduction of Indian continental lithosphere constrained by Eocene-Oligocene magmatism in

697   northern Myanmar, Lithos, 348–349, 105211, doi:10.1016/j.lithos.2019.105211, 2019.

698   Li, Z.-H., Liu, M. and Gerya, T.: Lithosphere delamination in continental collisional orogens: A

699   systematic numerical study, J. Geophys. Res. Solid Earth, 121(7), 5186–5211,

700   doi:10.1002/2016JB013106, 2016.

701   Liu, H., Xiao, Y., Van den Kerkhof, A., Wang, Y., Zeng, L. and Guo, H.: Metamorphism and fluid

702   evolution of the Sumdo eclogite, Tibet: Constraints from mineral chemistry, fluid inclusions and

703   oxygen isotopes, J. Asian Earth Sci., 172(September 2018), 292–307, doi:10.1016/j.jseaes.2018.09.013,

704   2019.

705   Liu, Y., Santosh, M., Yuan, T., Li, H. and Li, T.: Reduction of buried oxidized oceanic crust during

706   subduction, Gondwana Res., 32, 11–23, doi:10.1016/j.gr.2015.02.014, 2016.

707   Lu, C., Mao, Z., Lin, J., Zhuravlev, K. K., Tkachev, S. N. and Prakapenka, V. B.: Elasticity of single-

708   crystal iron-bearing pyrope up to 20 GPa and 750 K, Earth Planet. Sci. Lett., 361, 134–142,

709   doi:10.1016/j.epsl.2012.11.041, 2013.

710   Ma, L., Wang, B.-D., Jiang, Z.-Q., Wang, Q., Li, Z.-X., Wyman, D. A., Zhao, S.-R., Yang, J.-H., Gou,

711   G.-N. and Guo, H.-F.: Petrogenesis of the Early Eocene adakitic rocks in the Napuri area, southern

712   Lhasa: Partial melting of thickened lower crust during slab break-off and implications for crustal

713   thickening in southern Tibet, Lithos, 196–197, 321–338, doi:10.1016/j.lithos.2014.02.011, 2014.

714   Matchette-Downes, H., van der Hilst, R. D., Gilligan, A. and Priestley, K.: Seismological constraints

715   on the density, thickness and temperature of the lithospheric mantle in southwestern Tibet, Earth Planet.

716   Sci. Lett., 524, 115719, doi:10.1016/j.epsl.2019.115719, 2019.

717   Meng, Y., Weidner, D. J. and Fei, Y.: Deviatoric stress in a quasi-hydrostatic diamond anvil cell:

718   Effect on the volume-based pressure calibration, Geophys. Res. Lett., 20(12), 1147–1150,

719   doi:10.1029/93GL01400, 1993.

720   Milani, S., Nestola, F., Alvaro, M., Pasqual, D., Mazzucchelli, M. L., Domeneghetti, M. C. and Geiger,

721   C. A.: Diamond–garnet geobarometry: The role of garnet compressibility and expansivity, Lithos, 227,

722   140–147, doi:10.1016/j.lithos.2015.03.017, 2015.

723   Milani, S., Angel, R. J., Scandolo, L., Mazzucchelli, M. L., Ballaran, T. B., Klemme, S., Domeneghetti,

724   M. C., Miletich, R., Scheidl, K. S., Derzsi, M., Tokár, K., Prencipe, M., Alvaro, M. and Nestola, F.:

725   Thermo-elastic behavior of grossular garnet at high pressures and temperatures, Am. Mineral., 102(4),

726   851–859, doi:10.2138/am-2017-5855, 2017.

727   Miller, C., Schuster, R., Klotzli, U., Frank, W. and Purtscheller, F.: Post-Collisional Potassic and

Ultrapotassic Magmatism in SW Tibet: Geochemical and Sr-Nd-Pb-O Isotopic Constraints for Mantle

Source Characteristics and Petrogenesis, J. Petrol., 40(9), 1399–1424, doi:10.1093/petroj/40.9.1399,

1999.

Morency, C.: Numerical simulations of the mantle lithosphere delamination, J. Geophys. Res., 109(B3),

B03410, doi:10.1029/2003JB002414, 2004.

Nábělek, P. I. and Nábělek, J. L.: Thermal characteristics of the Main Himalaya Thrust and the Indian

lower crust with implications for crustal rheology and partial melting in the Himalaya orogen, Earth

Planet. Sci. Lett., 395, 116–123, doi:10.1016/j.epsl.2014.03.026, 2014.

Nishihara, Y., Takahashi, E., Matsukage, K. and Kikegawa, T.: Thermal equation of state of omphacite,

Am. Mineral., 88(1), 80–86, doi:10.2138/am-2003-0110, 2003.

Nomade, S., Renne, P. R., Mo, X., Zhao, Z. and Zhou, S.: Miocene volcanism in the Lhasa block, Tibet:

spatial trends and geodynamic implications☆, Earth Planet. Sci. Lett., 221(1–4), 227–243,

doi:10.1016/S0012-821X(04)00072-X, 2004.

Pandolfo, F., Nestola, F., Cámara, F. and Domeneghetti, M. C.: High-pressure behavior of space group

P2/n omphacite, Am. Mineral., 97(2–3), 407–414, doi:10.2138/am.2012.3928, 2012a.

Pandolfo, F., Nestola, F., Cámara, F. and Domeneghetti, M. C.: New thermoelastic parameters of

natural C2/c omphacite, Phys. Chem. Miner., 39(4), 295–304, doi:10.1007/s00269-012-0484-1, 2012b.

Panza, G. F., Brandmayr, E. and Romanelli, F.: A geophysical perspective on the lithosphere–

asthenosphere system from Periadriatic to the Himalayan areas: the contribution of gravimetry, Rend.

Lincei, 31(0123456789), 59–67, doi:10.1007/s12210-020-00892-z, 2020.

Pavese, A., Diella, V., Pischedda, V., Merli, M., Bocchio, R. and Mezouar, M.: Pressure-volume-

temperature equation of state of andradite and grossular, by high-pressure and -temperature powder

diffraction, Phys. Chem. Miner., 28(4), 242–248, doi:10.1007/s002690000144, 2001.

Peng, M., Jiang, M., Li, Z.-H., Xu, Z., Zhu, L., Chan, W., Chen, Y., Wang, Y., Yu, C., Lei, J., Zhang, L., Li, Q. and Xu, L.: Complex Indian subduction style with slab fragmentation beneath the Eastern Himalayan Syntaxis revealed by teleseismic P-wave tomography, Tectonophysics, 667, 77–86, doi:10.1016/j.tecto.2015.11.012, 2016.

Qin, F., Wu, X., Wang, Y., Fan, D., Qin, S., Yang, K., Townsend, J. P. and Jacobsen, S. D.: High-pressure behavior of natural single-crystal epidote and clinozoisite up to 40 GPa, Phys. Chem. Miner., 43(9), 649–659, doi:10.1007/s00269-016-0824-7, 2016.

Ren, Y. and Shen, Y.: Finite frequency tomography in southeastern Tibet: Evidence for the causal relationship between mantle lithosphere delamination and the north–south trending rifts, J. Geophys. Res., 113(B10), B10316, doi:10.1029/2008JB005615, 2008.

Rivers, M., Prakapenka, V., Kubo, A., Pullins, C., Holl, C. and Jacobsen, S.: The COMPRES/GSECARS gas-loading system for diamond anvil cells at the Advanced Photon Source, High Press. Res., 28(3), 273–292, doi:10.1080/08957950802333593, 2008.

Robertson, E. C.: Thermal properties of rocks., 1988.

Schulte-Pelkum, V., Monsalve, G., Sheehan, A., Pandey, M. R., Sapkota, S., Bilham, R. and Wu, F.: Imaging the Indian subcontinent beneath the Himalaya, Nature, 435(7046), 1222–1225, doi:10.1038/nature03678, 2005.

Semprich, J., Simon, N. S. C. and Podladchikov, Y. Y.: Density variations in the thickened crust as a function of pressure, temperature, and composition, Int. J. Earth Sci., 99(7), 1487–1510, doi:10.1007/s00531-010-0557-7, 2010.

Shi, D., Zhao, W., Klemperer, S. L., Wu, Z., Mechie, J., Shi, J., Xue, G. and Su, H.: West–east

transition from underplating to steep subduction in the India–Tibet collision zone revealed by receiver-function profiles, Earth Planet. Sci. Lett., 452, 171–177, doi:10.1016/j.epsl.2016.07.051, 2016.

Shi, D., Klemperer, S. L., Shi, J., Wu, Z. and Zhao, W.: Localized foundering of Indian lower crust in the India-Tibet collision zone, Proc. Natl. Acad. Sci. U. S. A., 117(40), 24742–24747, doi:10.1073/pnas.2000015117, 2020a.

Shi, Y.-N., Niu, F., Li, Z.-H. and Huangfu, P.: Craton destruction links to the interaction between subduction and mid-lithospheric discontinuity: Implications for the eastern North China Craton, Gondwana Res., 83, 49–62, doi:10.1016/j.gr.2020.01.016, 2020b.

Singh, A. and Kumar, M. R.: Seismic signatures of detached lithospheric fragments in the mantle beneath eastern Himalaya and southern Tibet, Earth Planet. Sci. Lett., 288(1–2), 279–290, doi:10.1016/j.epsl.2009.09.031, 2009.

Singh, H. and Mahatsente, R.: Lithospheric Structure of Eastern Tibetan Plateau from Terrestrial and Satellite Gravity Data Modeling: Implication for Asthenospheric Underplating, edited by S. Roeske, Lithosphere, 2020(1), doi:10.2113/2020/8897964, 2020.

Skinner, B. J.: Section 6: Thermal expansion, in Handbook of Physical Constants, pp. 75–96, Geological Society of America., 1966.

Tang, Y., Qin, Y., Gong, X., Duan, Y., Chen, G., Yao, H., Liao, J., Liao, S., Wang, D. and Wang, B.: Discovery of eclogites in Jinsha River suture zone, Gonjo County, eastern Tibet and its restriction on Paleo-Tethyan evolution, China Geol., 3(1), 83–103, doi:10.31035/cg2020003, 2020.

Turner, S., Hawkesworth, C., Liu, J., Rogers, N., Kelley, S. and van Calsteren, P.: Timing of Tibetan uplift constrained by analysis of volcanic rocks, Nature, 364(6432), 50–54, doi:10.1038/364050a0, 1993.

794   Wang, C., Zhao, X., Liu, Z., Lippert, P. C., Graham, S. A., Coe, R. S., Yi, H., Zhu, L., Liu, S. and Li,

795   Y.: Constraints on the early uplift history of the Tibetan Plateau, Proc. Natl. Acad. Sci., 105(13), 4987–

796   4992, doi:10.1073/pnas.0703595105, 2008.

797   Wang, C., Chen, W.-P. and Wang, L.-P.: Temperature beneath Tibet, Earth Planet. Sci. Lett., 375, 326–

798   337, doi:10.1016/j.epsl.2013.05.052, 2013.

799   Wang, Q., Wyman, D.A., Li, Z.X., Sun, W., Chung, S.L., Vasconcelos, P.M., Zhang, Q.Y., Dong, H.,

800   Yu, Y.S., Pearson, N., Qiu, H.N., Zhu, T.X.: Eocene north–south trending dikes in central Tibet: new

801   constraints on the timing of east. Earth and Planetary Science Letters 298 (1–2), 205–21,

802   doi:10.1016/j.epsl.2010.07.046, 2010.

803   Wang, X., Holt, W. E. and Ghosh, A.: Joint modeling of lithosphere and mantle dynamics: Sensitivity

804   to viscosities within the lithosphere, asthenosphere, transition zone, and D“ layers, Phys. Earth Planet.

805   Inter., 293(March), 106263, doi:10.1016/j.pepi.2019.05.006, 2019.

806   Wittlinger, G., Farra, V., Hetényi, G., Vergne, J. and Nábělek, J.: Seismic velocities in Southern Tibet

807   lower crust: a receiver function approach for eclogite detection, Geophys. J. Int., 177(3), 1037–1049,

808   doi:10.1111/j.1365-246X.2008.04084.x, 2009.

809   Xu, J., Zhang, D., Dera, P., Zhang, B. and Fan, D.: Experimental evidence for the survival of augite to

810   transition zone depths, and implications for subduction zone dynamics, Am. Mineral., 102(7), 1516–

811   1524, doi:10.2138/am-2017-5959, 2017.

812   Xu, J., Zhang, D., Fan, D., Zhang, J. S., Hu, Y., Guo, X., Dera, P. and Zhou, W.: Phase Transitions in

813   Orthoenstatite and Subduction Zone Dynamics: Effects of Water and Transition Metal Ions, J. Geophys.

814   Res. Solid Earth, 123(4), 2723–2737, doi:10.1002/2017JB015169, 2018.

815   Xu, J., Zhang, D., Fan, D., Dera, P. K., Shi, F. and Zhou, W.: Thermoelastic Properties of Eclogitic

816   Garnets and Omphacites: Implications for Deep Subduction of Oceanic Crust and Density Anomalies

817   in the Upper Mantle, Geophys. Res. Lett., 46(1), 179–188, doi:10.1029/2018GL081170, 2019.

818   Xu, J., Fan, D., Zhang, D., Li, B., Zhou, W. and Dera, P. K.: Investigation of the crystal structure of

819   low water content hydrous olivine to 29.9 GPa: a high-pressure single-crystal X-ray diffraction study,

820   Am. Mineral., doi:10.2138/am-2020-7444, 2020a.

821   Xu, J., Fan, D., Zhang, D., Guo, X., Zhou, W. and Dera, P. K.: Phase Transition of Enstatite-Ferrosilite

822   Solid Solutions at High Pressure and High Temperature: Constraints on Metastable Orthopyroxene in

823   Cold Subduction, Geophys. Res. Lett., 47(12), 1–10, doi:10.1029/2020GL087363, 2020b.

824   Yang, J., Xu, Z., Li, Z., Xu, X., Li, T., Ren, Y., Li, H., Chen, S. and Robinson, P. T.: Discovery of an

825   eclogite belt in the Lhasa block, Tibet: A new border for Paleo-Tethys?, J. Asian Earth Sci., 34(1), 76–

826   89, doi:10.1016/j.jseaes.2008.04.001, 2009.

827   Yang, Y., Abart, R., Yang, X., Shang, Y., Ntaflos, T. and Xu, B.: Seismic anisotropy in the Tibetan

828   lithosphere inferred from mantle xenoliths, Earth Planet. Sci. Lett., 515, 260–270,

829   doi:10.1016/j.epsl.2019.03.027, 2019.

830   Ye, Z., Fan, D., Tang, Q., Xu, J., Zhang, D. and Zhou, W.: Constraining the density evolution during

831   destruction of the lithospheric mantle in the eastern North China Craton, Gondwana Res., 91, 18–30,

832   doi:10.1016/j.gr.2020.12.001, 2021.

833   Zhai, Q., Zhang, R., Jahn, B., Li, C., Song, S. and Wang, J.: Triassic eclogites from central Qiangtang,

834   northern Tibet, China: Petrology, geochronology and metamorphic P–T path, Lithos, 125(1–2), 173–

835   189, doi:10.1016/j.lithos.2011.02.004, 2011a.

836   Zhai, Q., Jahn, B., Zhang, R., Wang, J. and Su, L.: Triassic Subduction of the Paleo-Tethys in northern

837   Tibet, China: Evidence from the geochemical and isotopic characteristics of eclogites and blueschists

838   of the Qiangtang Block, J. Asian Earth Sci., 42(6), 1356–1370, doi:10.1016/j.jseaes.2011.07.023,

839   2011b.

840   Zhang, D., Hu, Y. and Dera, P. K.: Compressional behavior of omphacite to 47 GPa, Phys. Chem.

841   Miner., 43(10), 707–715, doi:10.1007/s00269-016-0827-4, 2016.

842   Zhang, D., Dera, P. K., Eng, P. J., Stubbs, J. E., Zhang, J. S., Prakapenka, V. B. and Rivers, M. L.:

843   High Pressure Single Crystal Diffraction at PX^2, J. Vis. Exp., 2017(119), 1–9, doi:10.3791/54660,

844   2017a.

845   Zhao, M.-S., Chen, Y.-X. and Zheng, Y.-F.: Geochemical evidence for forearc metasomatism of

846   peridotite in the Xigaze ophiolite during subduction initiation in Neo-Tethyan Ocean, south to Tibet,

847   Lithos, 380–381, 105896, doi:10.1016/j.lithos.2020.105896, 2021.

848   Zhu, D.-C., Wang, Q., Zhao, Z.-D., Chung, S.-L., Cawood, P. A., Niu, Y., Liu, S.-A., Wu, F.-Y. and

849   Mo, X.-X.: Magmatic record of India-Asia collision, Sci. Rep., 5(1), 14289, doi:10.1038/srep14289,

850   2015.

851   Zou, Y., Gréaux, S., Irifune, T., Whitaker, M. L., Shinmei, T. and Higo, Y.: Thermal equation of state

852   of $Mg_3Al_2Si_3O_{12}$ pyrope garnet up to 19 GPa and 1700 K, Phys. Chem. Miner., 39(7), 589–598,

853   doi:10.1007/s00269-012-0514-z,   2012.

854 **Figure:**
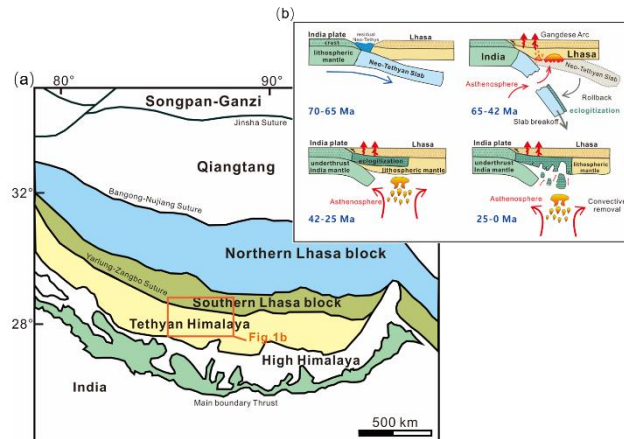
855

856 **Figure 1.** (a) Schematic geological map of the Tibetan Plateau (modified from Chung et al. 2005

857 and Wang et al. 2010). (b) Interpretive geological cartoon of India-Asia collision evolution. 70-65

858 Ma: The flat Neo-Tethyan oceanic slab subducts beneath Tibet with the closure of the Neo-Tethys

859 Ocean. 65-42 Ma: The rollback of the Neo-Tethyan slab breaks off after densification by

860 eclogitization. 42-25 Ma: The subduction of the Indian continent continued at a low subduction

861 angle beneath the Lhasa terrane and was accompanied by heavy thermal perturbation. 25-0 Ma:

862 The thickened eclogitic lower crust undergoes the "convective removal" of delamination due to

863 gravitational instability.

864

865
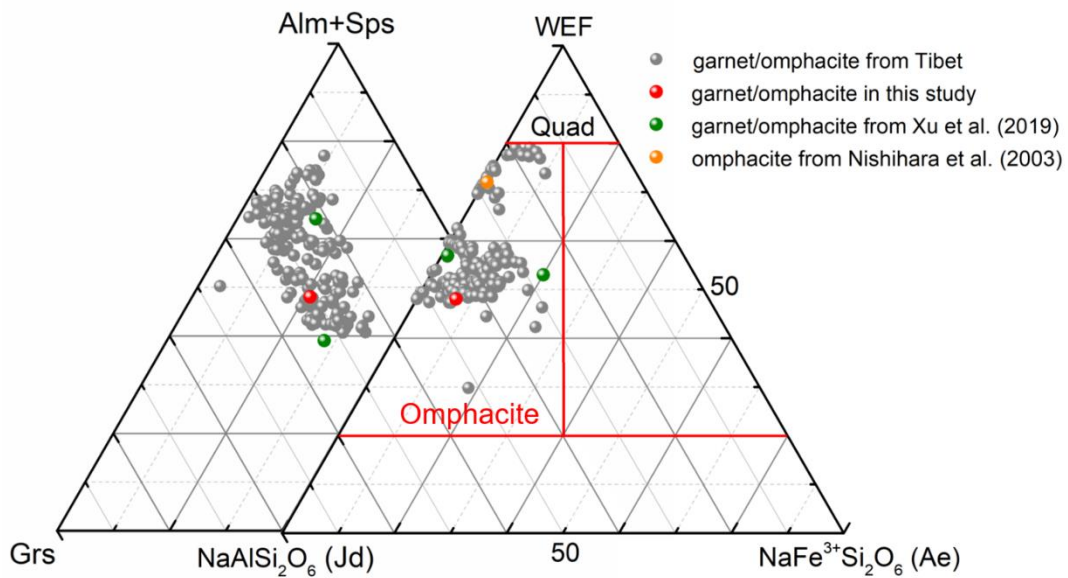
Figure 2. Composition of garnet and omphacite in eclogites from Tibet and this study. The gray

solid circles represent the components of garnet and omphacite collected from previous studies in

Tibet (e.g. Chan et al., 2009; Liu et al., 2019; Song et al., 2003; Weller et al., 2016; Yang et al.,

2009; Zhai et al., 2011a). The green solid circles are garnet and omphacite with different Fe

contents according to Xu et al. (2019). The orange solid circles are omphacite according to

Nishihara et al. (2003). The red solid circles are the components of garnet and omphacite in this

study. Prp = pyrope, Alm = almandine, Grs = grossular, Sps = spessartine, Quad = Ferrosilite +

enstatite + wollastonite, Jd = jadeite, and Ae = aegirine.

874
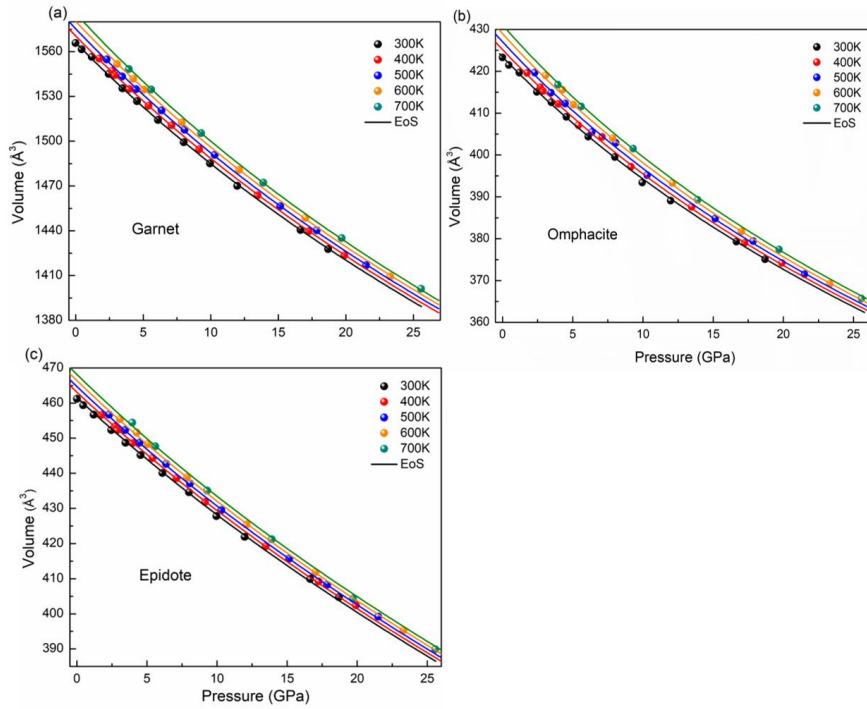
Figure 3. Pressure-volume-temperature relations of garnet (a), omphacite (b), and epidote (c).

Isothermal compression curves are calculated by using the thermoelastic parameters obtained in

this study.
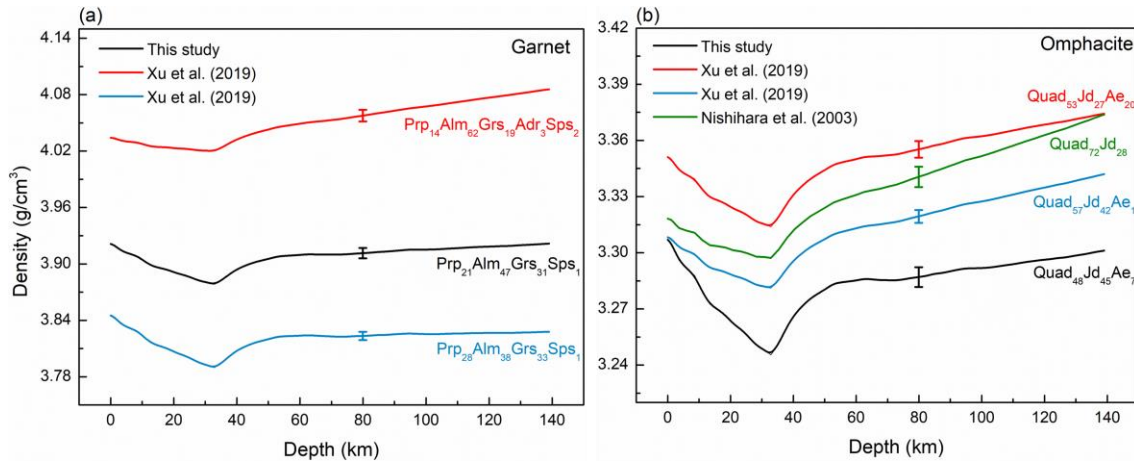
Figure 4. Density profiles of garnet (a) and omphacite (b) along with the cold Tibetan geothermal

line (Wang et al., 2013). The garnets of $Prp_{21}Alm_{47}Grs_{31}Sps_1$ and $Prp_{28}Alm_{38}Grs_{33}Sps_1$ are from

Xu et al. (2019). The omphacites of $Quad_{53}Jd_{27}Ae_{20}$ and $Quad_{57}Jd_{42}Ae_1$ are from Xu et al. (2019)

and $Quad_{72}Jd_{28}$ is from Nishihara et al. (2003).
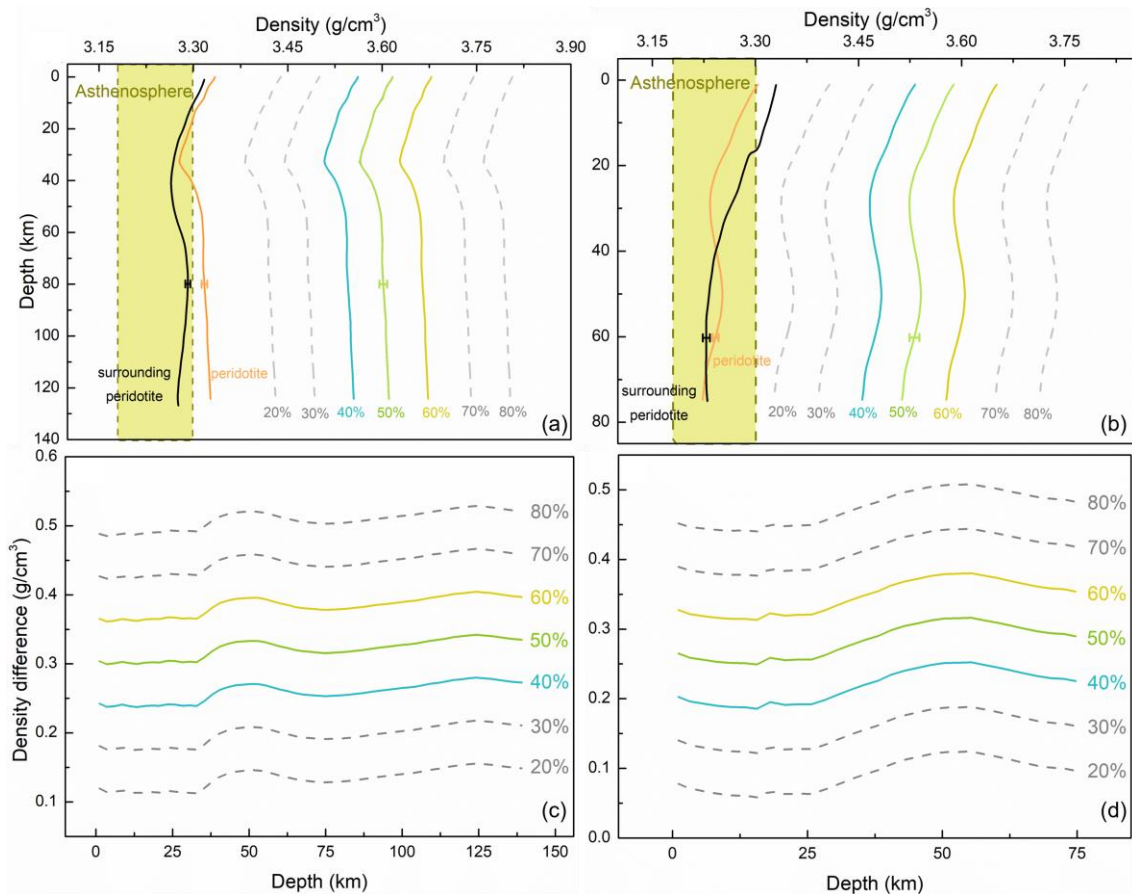
Figure 5. Density profiles of eclogite and peridotite assemblages ((a) and (b)) and density

difference between eclogite and peridotite ((c) and (d)) in Tibet along the Paleozoic and Cenozoic

geothermal lines under the conditions of Neo-Tethyan oceanic slab detachment (a) (Wang et al.,

2013) and subduction of the Indian continental margin beneath the Lhasa terrane (b) (Craig et al.,

2020). The percentage represents the content of garnet in eclogite, of which epidote accounts for 5

vol. % by default. The orange curve and black curve show the density profile of peridotite with a

composition of 70 vol. % olivine + 25 vol. % orthopyroxene + 3 vol. % clinopyroxene + 2 vol. %

spinel. The orange line shows the density of peridotite in the lithospheric mantle along the

Paleozoic (a) (Wang et al., 2013) and Cenozoic (b) (Craig et al., 2020) geothermal lines, and the

black curve indicates that the density of peridotite in the surrounding lithospheric mantle is along

the Paleozoic (a) (Nábělek and Nábělek, 2014) and Cenozoic (b) (Wang et al., 2013) geothermal

896   lines in Tibet. The shaded region is the density range of the asthenosphere (Chen and Tenzer, 2019;

897   Levin, 2006; Panza et al., 2020; Singh and Mahatsente, 2020).

898

899
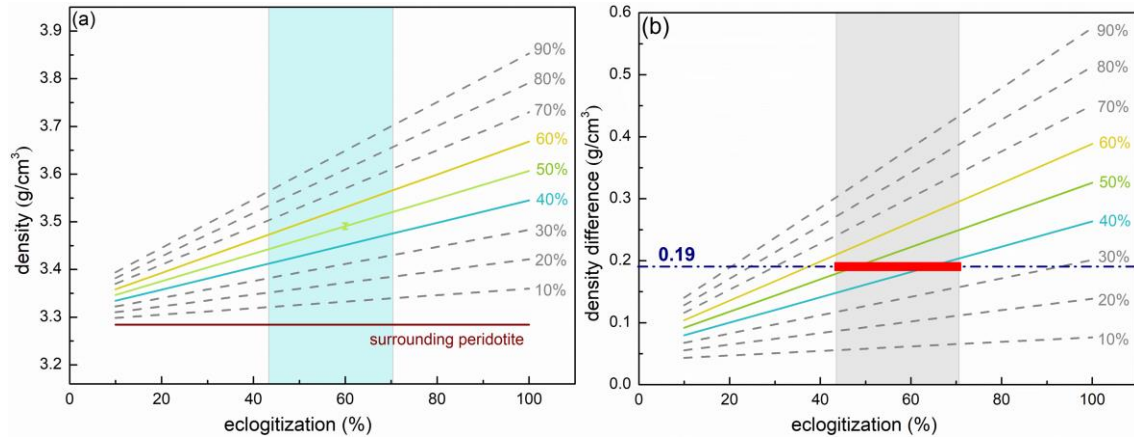
Figure 6. (a) The effect of eclogitization on the density of the subducted slab at ~80 km (2.6 GPa

and 625 °C) along the Paleozoic geothermal line. The percentage on the right represents the

content of garnet and the content of epidote is fixed at 5 vol. % by default. The content of garnets

in Tibet is between 40 vol. % and 60 vol. %. The density represents the average density of the

subducted slab with the entire eclogitic ocean lower crust and partially eclogitized lithospheric

mantle, where the degree of eclogitization refers to the lithospheric mantle. The rufous line

represents the average density of surrounding peridotite in this study. The blue shading indicates

the possible degree of eclogitization. (b) Density difference between eclogite with different

degrees of eclogitization and surrounding peridotite. The red dashed solid line represents a density

excess of 0.19 g/cm^3 from the isostatic balance and the geoid anomaly (Matchette-Downes et al.,

2019).